RSC Advances

PAPER

View Article Online
View Journal | View Issue

Cite this: *RSC Adv.*, 2017, **7**, 47938

Flux growth and characterization of an $FeSi_4P_4$ single crystal†

Tongtong Yu,[a] Shanpeng Wang,*[ab] Huapeng Ruan,[a] Chunlong Li,[a] Xixia Zhang,[a] Ning Jia,[a] Jian Zhang[ab] and Xutang Tao *[ab]

Received 23rd July 2017
Accepted 18th September 2017

DOI: 10.1039/c7ra08118a

rsc.li/rsc-advances

Herein, a single crystal of $FeSi_4P_4$ (FSP) with dimensions up to 8 × 7 × 3 mm^3 was successfully grown using a seeded flux growth method. Single crystal X-ray diffraction results revealed that the FSP crystal crystallized in the chiral space group *P*1 (no. 1). High-resolution X-ray diffraction presents a full-width at half-maximum (FWHM) of 36″ and 46″ for the (100) and (001) FSP crystals, respectively, which indicates that FSP crystals have high crystalline quality. FSP is thermally stable up to 1157.1 °C and has a high thermal conductivity of 35 W (m K)$^{-1}$ at room temperature. The magnetic analysis shows that the FSP crystal is paramagnetic in the range from 5 to 300 K. The Hall effect measurement suggests that the FSP crystal is a promising p-type semiconductor at room temperature.

Introduction

Due to the abundant structural chemistry and excellent physical properties of ternary silicon phosphides containing transition metals, extensive research has been carried out on their nonlinear optical and thermoelectric properties.[1–4] A number of representative ternary silicon phosphides have been reported such as $NiSi_2P_3$ (*Imm*2),[5] Si_3AlP (*Cc*),[6] $RhSi_3P_3$ and $IrSi_3P_3$ (*C*2),[7] $PtSi_2P_2$ ($P2_1$),[8] $LnSi_2P_6$ ($Cmc2_1$, Ln = La, Ce, and Pr),[9] and Ag_2SiP_2 ($I\bar{4}2d$).[10] Among these, the chalcopyrite structure II–IV–V_2 (II–Mg, Zn, Cd; IV–Si, Ge; and V–P, As) crystals, such as $CdSiP_2$ and $ZnGeP_2$, have great important applications in mid-infrared nonlinear optics owing to their outstanding nonlinear optical properties.[1,11] The $ZnSiP_2$ semiconductor is believed to be a promising candidate for applications in optoelectronics, spintronics, and quantum electronics.[12] Particularly, two room-temperature ferromagnetism semiconductors, $MnGeP_2$ and $MnGeAs_2$, have been researched in recent years.[13,14]

Perrier *et al.* systematically investigated transition metal phosphosilicides MSi_xP_y (M = Fe, Co, Ru, Rh, Pd, Os, Ir, and Pt).[8] $FeSi_4P_4$ (FSP) was identified as non-centrosymmetric by single X-ray diffraction and Raman spectroscopy. The magnetic analysis shows that it is paramagnetic at low temperatures (15–65 K) and diamagnetic at high temperatures.[8,15,16] Thus, it may be interesting that FSP is paramagnetic at low temperatures and transforms into a diamagnetic state at high temperatures. The thermal properties and electrical properties of the bulk crystal have not been reported.

In this study, to the best of our knowledge, large sized and high quality FSP crystals have been grown for the first time by a seeded flux growth method. Furthermore, the magnetic, electrical, and thermal properties of the bulk FSP crystal have been investigated.

Experimental

Crystal growth of FSP

Due to high saturated vapour pressure of phosphorus, silica ampoules tend to explode at high temperatures. The FSP compound is very difficult to be synthesized using a direct solid-state reaction method, and Sn flux growth method is adopted since it does not require special high pressure equipment and requires relatively low growth temperature. High purity elemental ferrum (4N), silicon (5N), phosphorus (6N), and tin (5N) were used as the starting materials. These starting materials were sealed in an evacuated silica ampoule with a ratio of Fe : Si : P : Sn = 1 : 4 : 4 : 6.[15] The furnace was rapidly heated to 1150 °C at a rate of 48 °C per h and slowly cooled down to 1075 °C at a rate of 1 °C per h.[17] Small grains of FSP were acquired after the Sn flux was diluted in concentrated hydrochloric acid. Subsequently, the seeded flux growth method was used to obtain bulk crystals. The silica ampoule was reloaded by powder starting materials with the same proportions of Fe : Si : P : Sn = 1 : 4 : 4 : 6. Particularly, a few small FSP crystals were used as seeds, and excessive phosphorus (~1 g) was places in the growth ampoule. The ampoule was sealed off at a vacuum of 5 × 10^{-4} Pa. It was then placed in a pit furnace controlled by a temperature controller (SHIMADEN FP23). Typically, the heating program of the furnace was set as follows: first, rapid heating was

[a]State Key Laboratory of Crystal Materials, Institute of Crystal Materials, Shandong University, No. 27 Shanda South Road, Jinan, 250100, PR China. E-mail: wshp@sdu.edu.cn; txt@sdu.edu.cn; Fax: +86 531 88574135; Tel: +86 531 88364963

[b]Key Laboratory of Functional Crystal Materials and Device (Shandong University, Ministry of Education), No. 27 Shanda South Road, Jinan, 250100, PR China

† Electronic supplementary information (ESI) available. See DOI: 10.1039/c7ra08118a

carried out to 1150 °C at a rate of 48 °C per hour; when the temperature was close to 1150 °C, the heating rate was reduced to avoid overheating of the melt; for decomposition, the temperature was 1157.1 °C, as observed *via* the DSC and TG analysis (see Fig. S3†). The FSP was already saturated in the Sn solution at 1150 °C. Second, maintaining the temperature at 1150 °C for 20 hours was necessary to ensure complete reaction. Finally, the furnace was cooled down to around 1075 °C at a rate of 0.4 °C per hour. The ampoule was then taken out of the furnace at 1075 °C. After cooling down to room temperature, large sized and high quality bulk FSP crystals were obtained after removing the remaining tin using diluted hydrochloric acid. A small crystal obtained using the standard Sn flux method in our experiment is shown in Fig. 1(a). The crystal size is about $3 \times 2 \times 1$ mm^3. The crystal grown by the seeded flux method, as shown in Fig. 1(b), is about $8 \times 7 \times 3$ mm^3. In Perrier's work, crystals with the dimensions of about $0.2 \times 0.2 \times 0.2$ mm^3 were obtained. These small crystals were used for single crystal X-ray diffraction.

X-ray diffraction (XRD) characterization

Powder X-ray diffraction was performed using a Bruker-AXS D8 ADVANCE X-ray diffractometer equipped with a diffracted beam monochromator set for Cu Kα radiation ($\lambda = 1.54056$ Å) in the range of 20–80° (2θ), with a step size of 0.02° and a step time of 0.04 s at room temperature. The single-crystal X-ray diffraction data was obtained by a Bruker APEX-II SMART CCD diffractometer equipped with a D8 goniometer at room temperature using graphite-monochromated Mo Kα radiations of $\lambda = 0.71073$ Å within the ω scan method. From three sets of frames, initial lattice parameters and orientation matrices were determined. Data integration and cell refinement were performed through the INTEGRATE program in the APEX-II software, and numerical face-indexed absorption corrections were adopted using the SCALE program for the area detector.[18] A prism-shaped crystal with dimensions of $0.13 \times 0.07 \times 0.03$ mm^3 knocked off a large crystal that was mounted on a glass fibre with epoxy. The structural model was refined using the SHELXL-97 routine (Sheldrick, 1997). Crystal data and refinement summaries are presented in Table 1.

High-resolution X-ray diffraction (HRXRD)

Herein, two (100) and (001)-faced FSP wafers with the dimensions of $4 \times 4 \times 1$ mm^3 were used for HRXRD characterization.

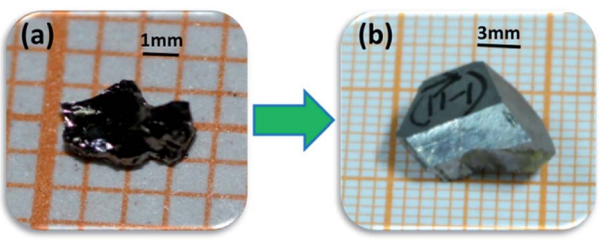

Fig. 1 The images of the bulk FSP single crystals (a) obtained using the standard flux method, and (b) seeded flux method. Each small square is 1 mm^2.

Table 1 Crystal data and structure refinement for FSP

Chemical formula	$FeSi_4P_4$
Crystal system	Triclinic
Color	Black
Space group	*P*1
Temperature (K)	296
a (Å)	4.892 (16)
b (Å)	5.5790 (18)
c (Å)	6.10 (2)
α (°)	85.25 (3)
β (°)	68.07 (3)
γ (°)	70.07 (3)
V (Å^3)	145.10 (8)
Z	1
F(000)	142
ρ (g cm^{-3})	3.344
Radiation type	Mo Kα, 0.71073 Å
θ	3.6–27.6°
μ (mm^{-1})	4.39
Crystal size (mm)	0.27 × 0.21 × 0.17
S	1.19
$R\ [I > 2\sigma_1]^a$	0.0230
$wR\ [I > 2\sigma_1]^a$	0.0538
Reflections/parameters	1312/83

^{a} $R = \sum||F_o| - |F_c||/\sum|F_o|$, $wR = [\sum[w(F_o^2 - F_c^2)^2]/\sum[w(F_o^2)^2]]^{1/2}$.

The opposite surfaces were mechanically polished carefully. HRXRD was performed using a Bruker-AXS D5005HR diffractometer with a four-crystal Ge (220) monochromator set for Cu Kα radiation ($\lambda = 0.15419$ nm). The step size and step time were 0.001° and 0.1 s, respectively. The setting of the generator was 40 kV and 20 mA.

Raman spectrum

The Raman spectrum was obtained in a back-scattering configuration by an HR 800 system from Horiba Jobin Yvon at room temperature, and a 632 nm laser was used as the excitation source. A polished crystal plate with the dimensions of $5 \times 3 \times 1$ mm^3 was used.

Energy-dispersive X-ray spectroscopy

A small crystal with the dimensions of about $2.5 \times 2 \times 1.5$ mm^3 was cut, and energy-dispersive X-ray spectroscopy (EDS) analysis was performed using a field emission scanning electron microscope (FE-SEM, Hitachi S-4800) with an energy dispersive X-ray spectrometer (EDS, Horiba EMAX Energy EX-350). The accelerating voltage was 15 kV.

X-ray photoelectron spectroscopy (XPS)

X-ray photoelectron spectra were obtained using an ESCALAB 250 spectrometer (Thermo Fisher Scientific) with monochromatized Al Kα X-ray radiation (1486.6 eV) under ultrahigh vacuum (<10^{-7} Pa). The size of the light spot was 500 μm. A survey scan has been applied from 0 eV to 1050 eV. A crystal wafer with the dimensions of $2.5 \times 3 \times 1.5$ mm^3 was used for XPS characterization.

Thermal properties

Thermal gravity analysis (TGA) and differential scanning calorimetry (DSC) were carried out using a TGA/DSC 1/1600HT analyser (Mettler-Toledo Inc.) using high purity argon as a protective atmosphere, and the gas flow rate was 80 ml min^{-1}. The samples were placed in an alumina crucible and heated from room temperature to 1200 °C at a rate of 10 °C min^{-1}. Thermal mechanical properties were investigated *via* TMA/SDTA 840 (Mettler-Toledo Inc.) using argon as an protective atmosphere, and the gas flow was 70 ml min^{-1}. The thermal conductivity was carried out using a laser conductometer (NETZSCH LFA457 MicroFlash). Herein, three FSP wafers along the directions *a*, *b*, and *c* were cut and roughly polished.

Magnetic properties

The data of magnetic properties were obtained using SQUID (superconducting quantum interference device, Quantum Design Inc.). The magnetic field was set as 1000 Oe. The temperature range was 5–300 K. FSP powder was prepared after being finely ground and soaked in diluted hydrochloric acid for two hours.

Hall effect and piezoelectric properties

The FSP crystal plates were cut into 4 × 4 × 1 mm^3. The electric properties data are obtained by the Hall effect with a magnetic field intensity of 3 tesla and current intensity of 1 mA using the SQUID equipment.

Results and discussion

The single crystal data and structural parameters are presented in Table 1. Fractional atomic coordinates, equivalent isotropic displacement parameters, atomic displacement parameters, bond lengths, and bond angles of the FSP crystal are listed in Tables S1–S4 (see in ESI†).

FSP crystallizes in a triclinic crystal system, with the space group *P*1 (no. 1). In the crystal structure, Fe atoms are octahedrally coordinated by P and Si atoms, as shown in Fig. 2(d). The P and Si atoms are tetrahedrally surrounded by Fe, P, and Si atoms. The non-metallic atom tetrahedron [SiP_4] overlaps with [PSi_4] tetrahedron, as shown in Fig. 2(c). The lengths of Si–P bonds in orthorhombic SiP_2 range from 2.2378(8) to 2.3217(14) Å.[19] The length of the Si–P bond in $CdSiP_2$ is 2.2469(7) Å.[1] Our results show that the lengths of Si–P bonds in FSP range from 2.2303(62) to 2.3233(72) Å, which is comparable with those in orthorhombic SiP_2 and $CdSiP_2$. The [$FeSi_3P_3$] octahedrons and overlapped tetrahedrons are linked by shared corners, as shown in Fig. 2(a) and (b).

The Rietveld refinement pattern of the FSP crystal is shown in Fig. 3. As can be seen from Fig. 3, the experimental data are in good agreement with the calculated data according to the crystal structure of FSP. Global *R* factors are $R_p = 4.08\%$ and $R_{wp} = 5.40\%$, where

$$R_p = \sum|Y_{oi} - Y_{ci}|/\sum Y_{oi}^2$$

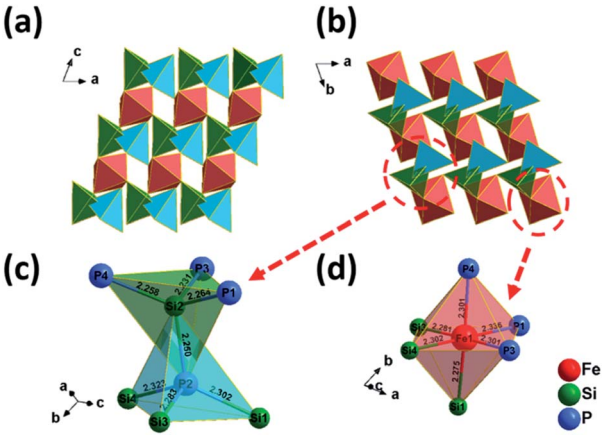

Fig. 2 (a) FSP crystal structure viewed along the *b*-axis. (b) FSP crystal structure viewed along the *c*-axis. (c) The overlapped [SiP_4] tetrahedron and [PSi_4] tetrahedron. (d) The [$FeSi_3P_3$] octahedron. Red atom represents iron, green atoms represent phosphorus, and blue atoms represent silicide. Light red octahedrons represent [$FeSi_3P_3$] octahedrons, green tetrahedrons represent [SiP_4] tetrahedrons, and light blue tetrahedrons represent [PSi_4] tetrahedrons.

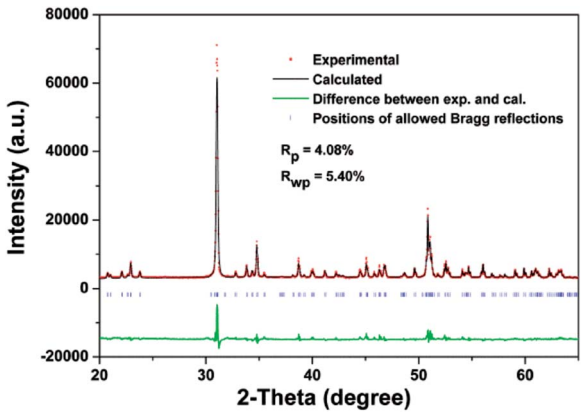

Fig. 3 Rietveld refinement pattern for the sample FSP crystal. Experimental (red dot), calculated (black line), and their difference (green trace). The tick marks (blue) indicate the positions of the allowed Bragg reflections.

$$R_{wp} = \sum[W_i(Y_{oi} - Y_{ci})^2/\sum W_i Y_{oi}^2]^{1/2}$$

Y_{oi} and Y_{ci} are the experimental and calculated intensities at each point in the pattern, respectively. W_i is the weight assigned to each step intensity.[20,21] The relatively low values of R_p and R_{wp} indicate that a high purity and single phase of FSP has been obtained.

The atom ratio of the FSP crystal is presented in the EDS spectrum (Fig. S1†). The ratio of Fe : Si : P is 11.08 : 43.16 : 45.77, which is approximately 1 : 4 : 4. No Sn flux was detected.

Since the structure symmetry of transition-metal silicon phosphides cannot be completely determined only by diffraction methods, Raman spectroscopy was performed to confirm the symmetry of FSP (Fig. 4). Herein, 23 Raman modes in the spectrum indicate the non-centrosymmetric structure of the

FSP crystal.[8] The lower-wavenumber Raman spectral lines, such as 250 cm^{-1}, are more intense. The low-wavenumber modes are assigned to the relative motions of octahedron [$FeSi_3P_3$] and tetrahedron ([SiP_4] and [PSi_4]) units. The Raman shifts of FSP are in good agreement with the previous results.[15] The narrow and well-defined peaks of the Raman shift as well as the low level of background proved the general good quality of the as-grown crystals.

HRXRD was performed to characterize the quality of the FSP crystal. The rocking curves of the (100) and (001)-FSP crystal are shown in Fig. 5. The peaks are symmetrical, and the full-width at half-maximum (FWHM) are 36″ and 46″, respectively. This indicates that the as-grown crystal is of high quality and integrity.

Thermal properties of FSP are shown in Fig. 6, 7, and S2.† A sharp fall in the DSC curve is observed at about 1157.1 °C together with the dramatic weight loss (Fig. S2†), indicating the decomposition of FSP. To protect the instrument, the instrument was shut down quickly when FSP started to decompose. In our crystal growth process, the actual growth temperature is 5–10 °C lower than the decomposition temperature. After several experiments, the optimum growth temperature was 1150 °C. When the temperature is up to 1150 °C, the solution system reaches saturation. FSP crystallizes on the surface of seed crystals and grows continuously with the decreasing temperature.

To investigate the thermal properties of the FSP crystals, three wafers along the *a*, *b*, and *c* directions were prepared. Thermal expansion and thermal conductivity curves along the three directions are presented in Fig. 6 and 7. Thermal conductivity is calculated by the following formula:

$$\kappa = \lambda \rho C_p$$

κ, λ, ρ, and C_p represent thermal conductivity, thermal diffusivity, the density of FSP, and specific heat at a constant pressure, respectively. The values of thermal diffusivity and constant pressure specific heat can be directly measured by the laser conductometer. This phenomenon indicates that the FSP crystal can tolerate more thermal load at room temperature. The thermal conductivity of FSP at room temperature is about

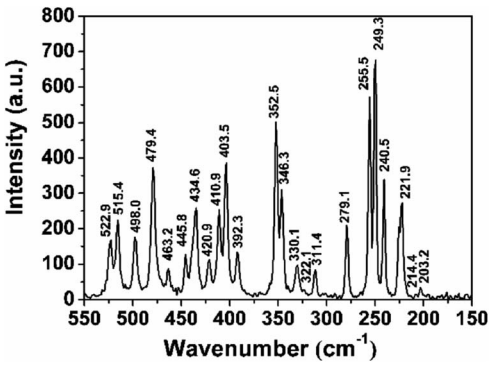

Fig. 4 Raman spectrum of the FSP crystal. There are 23 active modes in the spectrum, meaning that the FSP is non-cantered symmetric.

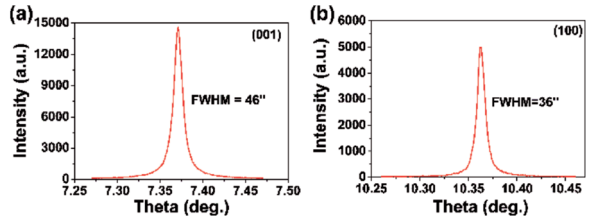

Fig. 5 Rocking curves of the (a) (001) and (b) (100)-FSP crystal. The acute and symmetric Rocking curves indicate that the as-grown FSP crystal is of high quality and integrity.

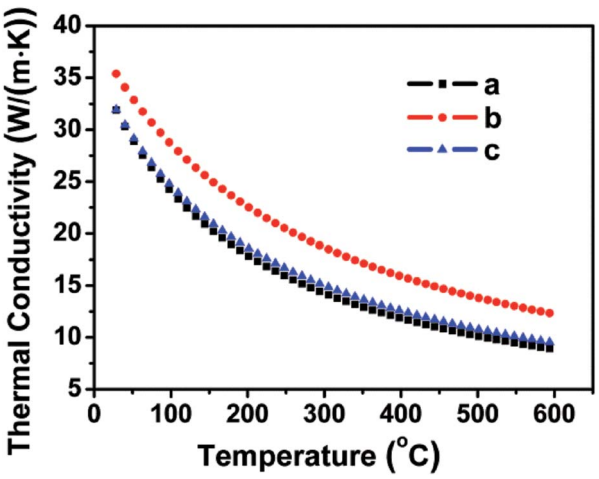

Fig. 6 Thermal conductivity curves of the FSP single crystal along the directions *a*, *b*, and *c*. The thermal conductivity of the FSP crystal descends with the increasing temperature.

35 W (m K)$^{-1}$, which is approximate to that of $ZnGeP_2$ (35 W (m K)$^{-1}$) and is higher than that of $CdSiP_2$ (13 W (m K)$^{-1}$). Both $ZnGeP_2$ and $CdSiP_2$ are excellent mid-infrared nonlinear optical materials with high thermal conductivity.[1,22] Other physical properties of FSP will be researched in our upcoming study. The solid lines in Fig. 7 are the thermal expansion ratio curves along the crystallographic axes. The average linear thermal expansion coefficient for the crystallographic directions can be calculated according to the following formula:

$$\alpha(T_0 \rightarrow T) = \frac{\Delta L}{L_0} \times \frac{1}{\Delta T}$$

where α is the average linear thermal expansion coefficient in the temperature range from T_0 to T, L_0 is the sample length at T_0, ΔL is the length change when the temperature changes from T_0 to T, and the temperature change is $\Delta T = T - T_0$.

The values of the average linear thermal expansion coefficients of the FSP crystal in the temperature range from 30 to 600 °C are $\alpha_a = 7.37 \times 10^{-6}\ K^{-1}$, $\alpha_b = 8.07 \times 10^{-6}\ K^{-1}$, and $\alpha_c = 7.37 \times 10^{-6}\ K^{-1}$. The weak anisotropy of the thermal expansion effectively protects the crystal from cracking caused by thermal expansion during crystal growth, processing, and applications.

The X-ray photoelectron spectroscopy (XPS) was carried out to determine the chemical valence of each element in the FSP crystal. The result is demonstrated in Fig. 8. No Sn 3d peaks are

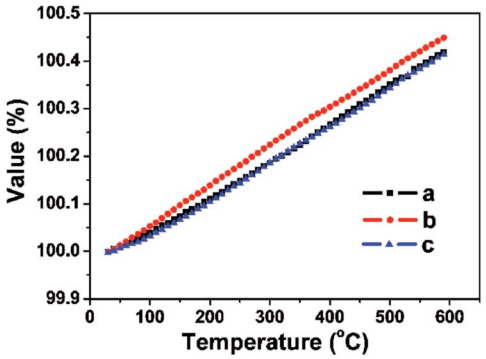

Fig. 7 Thermal expansion of the FSP crystal along the directions *a*, *b*, and *c*. It can be seen that the expansion ratio is almost linear over the entire measured temperature range, and the FSP crystal exhibits expansion upon heating.

found in the survey spectrum (Fig. 10(a)). The peaks of O 1s and C 1s are inevitable for the existence of carbon dioxide in the air. The binding energy (BE) of C 1s is set as 284.6 eV.[23] The peaks of Sc 2s, Sc 2p, Ca 2s, and Ca 2p are also labeled out in the spectrum. These impurities may originate from the instrument.

Fig. 8(b)–(d) show the profile of Fe 2p, Si 2p, and P 2p, respectively. The Fe 2p spectrum shows two peaks with the mean BE values at 712.8 eV and 724.3 eV, assigned to the Fe $2p_{3/2}$ and Fe $2p_{1/2}$ peaks, respectively. The valence state of Fe contains mixed +2 and +3 states.[24–27] The Si 2p peak can be clearly resolved into two splitting spin–orbits with the BE values of 103.5 eV and 104.2 eV, corresponding to the BE of Si $2p_{3/2}$ and Si $2p_{1/2}$, respectively. The single Si 2p peak in XPS indicates that there is only one oxidation state of Si in FSP. However, the accurate value of Si valence cannot be confirmed. The certain value of Si valence is in the range from +2.25 to +2.5.[28–30] The P 2p spectrum can also be resolved into two spin–orbits of 129.2 eV and 130.1 eV, corresponding to the BE of P $2p_{3/2}$ and P $2p_{1/2}$, respectively. This could be attributed to P^{3-} in FSP.[31,32]

The magnetization–temperature (*M*–*T*) curve (Fig. 9(a)) and the magnetization–field curve (Fig. 9(b)) of FSP reveal that the FSP crystal is paramagnetic in the temperature range of 5–300 K. The *M*–*H* curve is a straight line crossing the origin of

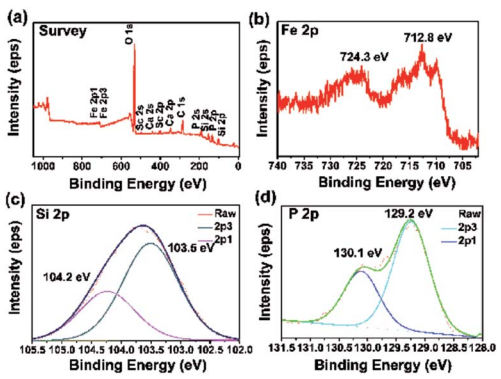

Fig. 8 (a) Survey, (b) Fe 2p, (c) Si 2p, and (d) P 2p spectrum of the FSP single crystal.

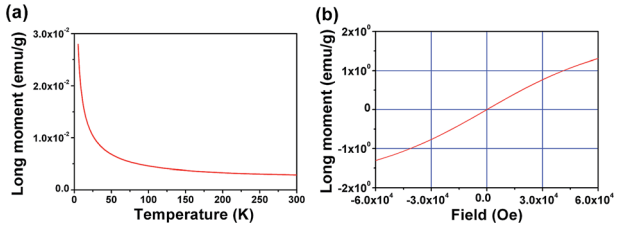

Fig. 9 (a) *M*–*T* curve of the FSP single crystal at a magnetic field strength of 1000 Oe. (b) *M*–*H* curve of FSP single crystal at a temperature of 5 K.

coordinates, and the value of the magnetization is above 0 and far less than 1. There is no phase transformation at low temperatures in this study. This is obviously different from the research suggesting that FSP is paramagnetic at low temperatures (15–65 K) and diamagnetic at high temperatures.[8] As is known, metal Sn is a type of diamagnetic material. Trace amounts of Sn are sufficient to influence the magnetic performance.[33] Therefore, trace amounts of Sn impurity in FSP might lead to the paramagnetic–diamagnetic phase transition at low temperatures. To figure out the reason of these contrary results, the FSP samples without being soaked in dilute hydrochloric acid were also investigated by XPS and SQUID.

As shown in Fig. S3,† there were trace amounts of Sn in the $FeSi_4P_4$ crystal when it was not soaked in dilute hydrochloric acid. Fig. S4† indicates that paramagnetic FSP transforms into diamagnetic FSP at a low temperature of 70 K; this agrees well with the reported results. Therefore, we believe that there is no paramagnetic-to-diamagnetic transition in the pure FSP crystal. However, the transition reported in the previous study[8] might be due to the trace amounts of Sn in the crystal.

As shown in Fig. S5,† the experiment data fit the Curie–Weiss law with an additional temperature-independent term χ_0,

$$\chi = C/(T - \theta) + \chi_0$$

The values of the Curie constant (C), Weiss constant (θ), and χ_0 are 9.71×10^{-4} emu K (g Oe)$^{-1}$, −4.43 K, and 2.08×10^{-6}

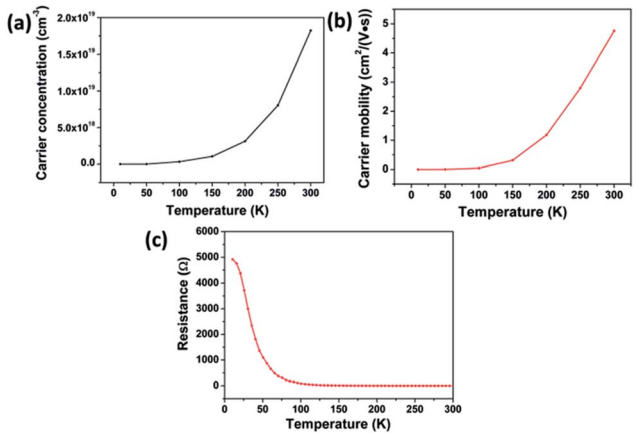

Fig. 10 The curves of temperature-dependent (a) carrier concentration, (b) carrier mobility, and (c) resistance.

emu (g Oe)$^{-1}$, respectively. The value of P_{eff} is calculated to be 1.51 μ_B using the Curie constant.[34] The reason for this value is likely to be the hybridization between Fe 3d states and Si 3sp states in the FSP crystal, similar to that observed in the $Mn_{1-x}Ni_xAl$ alloys.[35] In addition, the high carrier concentration can lead to the decrease in P_{eff}.[36,37] A small and negative Weiss constant indicates an antiferromagnetic exchange in FSP.[38] The antiferromagnetic exchange is associated with the interaction between Fe^{3+} and Fe^{2+}.[39]

The temperature-dependent resistance, carrier concentration, and carrier mobility curves are shown in Fig. 10. The FSP crystal is a p-type semiconductor with a resistivity of 0.124 Ω cm and a small gap energy of 0.15 eV at room temperature.[8] The carrier concentration is 1.83×10^{19} cm^{-3} at room temperature, and it decreases markedly with the decreasing temperature. The carrier mobility decreases and the resistance increases as the temperature decreases. FSP has a relatively high conductivity (35 W (m K)$^{-1}$), which is comparable to that of the well-known mid-infrared nonlinear optical $ZnGeP_2$.[40] The resistivity of FSP (0.124 Ω cm) is smaller than that of many other phosphorus silicides, such as $RhSi_3P_3$ (0.15 Ω cm) and $CoSi_3P_3$ (0.62 Ω cm), at room temperature.[8] Many researches indicate that certain kinds of transition metal phosphorus silicides have outstanding applications in integrated circuits technology because of their low resistivity and high thermal conductivity.[8,41] Other physical properties of FSP, such as optical properties, will be investigated in future.

Conclusions

Herein, the bulk FSP crystal with dimensions up to 8 × 7 × 3 mm^3 was successfully obtained using a seed flux method. Single-crystal X-ray diffraction results show that FSP crystallizes in the chiral space group $P1$ (no. 1) with the cell parameters a = 4.892(16) Å, b = 5.579(18) Å, c = 6.10(2) Å, α = 85.25(3)°, β = 68.07(3)°, and γ = 70.07(3)°, and the final R value is 0.023. Its thermal conductivity is high up to 35 W (m K)$^{-1}$ at room temperature. The experimental results indicate that there is no paramagnetic-to-diamagnetic transition in the pure FSP crystal. However, the transition reported in literature might due to the trace amounts of Sn in the crystal. The carrier concentration of FSP is 1.83×10^{19} cm^{-3}, the electric resistivity is 0.124 Ω cm, and the carrier mobility is 4.75 cm^2 (V s)$^{-1}$. FSP is a promising candidate for p-type conductor at room temperature.

Conflicts of interest

There are no conflicts to declare.

Acknowledgements

This work was partly supported by the National Natural Science Foundation of China (Grant No. 51572155, 51321091), the National Key Research and Development Program of China (Grant No. 2016YFB1102201), the Shandong Provincial Natural Science Foundation, China (ZR2014EMM015), and the Independent Innovation Foundation of Shandong University, IIFSDU.

Notes and references

1 G. Zhang, X. Tao, H. Ruan, S. Wang and Q. Shi, *J. Cryst. Growth*, 2012, **340**, 197–201.
2 G. A. Verozubova, A. I. Gribenyukov, V. V. Korotkova, O. Semchinova and D. Uffmann, *J. Cryst. Growth*, 2000, **213**, 334–339.
3 A. F. May, M. A. McGuire and H. Wang, *J. Appl. Phys.*, 2013, **113**, 103707.
4 P. Wang, F. Ahmadpour, T. Kolodiazhnyi, A. Kracher, L. M. D. Cranswick and Y. Mozharivskyj, *Dalton Trans.*, 2010, **39**, 1105–1112.
5 J. Wallinda and W. Jeitschko, *J. Solid State Chem.*, 1995, **114**, 476–480.
6 J.-H. Yang, H. Liu, *et al.*, *J. Am. Chem. Soc.*, 2012, **134**, 12653–12657.
7 J. Kreisel, O. Chaix-Pluchery, F. Genet, *et al.*, *J. Solid State Chem.*, 1997, **128**, 142–149.
8 C. Perrier, J. Kreisel, H. Vincent, O. Chaix-Pluchery and R. Madar, *J. Alloys Compd.*, 1997, **262–263**, 8.
9 K. Hopkins, J. T. Goldstein, D. E. Zelmon and C. A. Leininger, *Proceedings of the SPIE-The International Society for Optical Engineering*, 2005.
10 P. Kaiser and W. Jeitschko, *ChemInform*, 1997, **28**, 462–468.
11 G. Zhang, X. Tao, S. Wang, G. Liu, Q. Shi and M. Jiang, *J. Cryst. Growth*, 2011, **318**, 717–720.
12 Y. Zhang, *Comput. Mater. Sci.*, 2017, **133**, 152–158.
13 S. Cho, S. Choi, G.-B. Cha, S. C. Hong, Y. Kim, A. J. Freeman, J. B. Ketterson, Y. Park and H.-M. Park, *Solid State Commun.*, 2004, **129**, 609–613.
14 G.-B. Cha, W. S. Yun and S. C. Hong, *J. Magn. Magn. Mater.*, 2016, **419**, 202–209.
15 J. Kreisel, C. Perrier, H. Vincent, G. Lucazeau and A. R. Madar, *J. Raman. Spectrosc.*, 1999, **30**, 417–420.
16 C. Perrier, P. Chaudouet, *et al.*, *Mater. Res. Bull.*, 1995, **30**, 357–364.
17 C. Perrier, H. Vincent, P. Chaudou, B. Chenevier and A. R. Madar, *Mater. Res. Bull.*, 1995, **30**, 8.
18 *B. APEX2*, Bruker Analytical X-ray Instrument, Inc, Madison, WI, 2005.
19 X. Zhang, S. Wang, H. Ruan, G. Zhang and X. Tao, *Solid State Sci.*, 2014, **37**, 1–5.
20 E. Jansen, W. Schafer and G. Will, *J. Appl. Crystallogr.*, 1994, **6**, 492–496.
21 A. R. Lennie, S. A. T. Redfern, P. F. Schofield and D. J. Vaughan, *Mineral. Mag.*, 1995, **59**, 677–683.
22 G. Zhang, X. Tao, S. Wang, Q. Shi, H. Ruan and L. Chen, *J. Cryst. Growth*, 2012, **352**, 67–71.
23 V. V. Atuchini, V. G. Kesler and A. O. V. Parasyuk, *Surf. Rev. Lett.*, 2007, **14**, 403–409.
24 T. K. Chattopadhyay and H. G. Von Schnering, *Z. Kristallogr.–Cryst. Mater.*, 1984, **167**, 1–12.
25 C. Yang, G. Wang, Z. Lu, J. Sun, J. Zhuang and W. Yang, *J. Mater. Chem.*, 2005, **15**, 4252.

26 L. Bartolome, M. Imran, K. G. Lee, A. Sangalang, J. K. Ahn and D. H. Kim, *Green Chem.*, 2014, **16**, 279–286.
27 J. R. A. Carlsson, L. D. Madsen, M. P. Johansson, L. Hultman, X. H. Li, H. T. G. Hentzell and L. R. Wallenberg, *J. Vac. Sci. Technol., A*, 1997, **15**, 394–401.
28 A. Cros, R. Saoudi, G. Hollinger, C. A. Hewett and S. S. Lau, *J. Appl. Phys.*, 1990, **67**, 1826–1830.
29 E. Paparazzo, *J. Electron Spectrosc. Relat. Phenom.*, 1987, **43**, 97–112.
30 E. Paparazzo and M. Fanfoni, *Appl. Surf. Sci.*, 1992, **56–58**, 866–872.
31 R. Franke, T. Chasse, P. Streubel and A. Meisel, *J. Electron Spectrosc. Relat. Phenom.*, 1991, **56**, 381–388.
32 T. P. Moffat, R. M. Latanision and R. R. Ruf, *Electrochim. Acta*, 1995, **40**, 1723–1734.
33 J. A. Aitken, G. M. Tsoi, L. E. Wenger and S. L. Brock, *Chem. Mater.*, 2007, **19**, 5272–5278.
34 G. V. Bazuev, A. P. Tyutyunnik, M. V. Kuznetsov and R. P. Samigullina, *Eur. J. Inorg. Chem.*, 2016, **2016**, 5340–5346.
35 V. Rednic, M. Coldea, S. K. Mendiratta, M. Valente, V. Pop, M. Neumann and L. Rednic, *J. Magn. Magn. Mater.*, 2009, **321**, 3415–3421.
36 D. Gao, J. Zhang, J. Zhu, J. Qi, Z. Zhang, W. Sui, H. Shi and D. Xue, *Nanoscale Res. Lett.*, 2010, **5**, 769–772.
37 L.-H. Ye and A. J. Freeman, *Phys. Rev. B: Condens. Matter Mater. Phys.*, 2006, **73**, 081304.
38 L.-H. Bi, U. Kortz, M. H. Dickman, S. Nellutla, N. S. Dalal, B. Keita, L. Nadjo, M. Prinz and M. Neumann, *J. Cluster Sci.*, 2006, **17**, 143–165.
39 M. A. Salim, G. D. Khattak, P. S. Fodor and L. E. Wenger, *J. Non-Cryst. Solids*, 2001, **289**, 185–195.
40 Z. Lei, C. Zhu, C. Xu, B. Yao and C. Yang, *J. Cryst. Growth*, 2014, **389**, 23–29.
41 H. Vincent, J. Kreisel, Ch. Perrier, O. Chaix-Pluchery, P. Chaudouet, R. Madar, F. Genet and A. G. Lucazeau, *J. Solid State Chem.*, 1996, **124**, 7.